Performances of an 80–200 kV microscope employing a cold-FEG and an aberration-corrected objective lens

Christian Ricolleau, Jaysen Nelayah, Tetsuo Oikawa, Yuji Kohno, Nadi Braidy, Guillaulle Wang, Florian Hue, Lenuta Florea, Véronique Pierron Bohnes, Damien Alloyeau

▶ **To cite this version:**

Christian Ricolleau, Jaysen Nelayah, Tetsuo Oikawa, Yuji Kohno, Nadi Braidy, et al.. Performances of an 80–200 kV microscope employing a cold-FEG and an aberration-corrected objective lens. Probe Microscopy, 2013, 62 (2), pp.283-293. 10.1093/jmicro/dfs072 . hal-04277302

HAL Id: hal-04277302
https://hal.science/hal-04277302v1

Submitted on 9 Nov 2023

HAL is a multi-disciplinary open access archive for the deposit and dissemination of scientific research documents, whether they are published or not. The documents may come from teaching and research institutions in France or abroad, or from public or private research centers.

L'archive ouverte pluridisciplinaire **HAL**, est destinée au dépôt et à la diffusion de documents scientifiques de niveau recherche, publiés ou non, émanant des établissements d'enseignement et de recherche français ou étrangers, des laboratoires publics ou privés.

Performances of an 80 – 200 kV microscope employing a cold-FEG and an aberration-corrected objective lens

C. Ricolleau[1)], J. Nelayah[1)], T. Oikawa[1, 2)], Y. Kohno[2)], N. Braidy[1,3,*)], G. Wang[1)], F. Hue[1,**)], I. Florea[4)], V. Pierron Bohnes[4)], D. Alloyeau[1)]

1) Laboratoire Matériaux et Phénomènes Quantiques, Université Paris 7/CNRS, UMR 7162, Case 7021, 75205 Paris Cedex 13, France

2) JEOL Ltd., 1-2 Musashino 3-chome, Akishima, 196-8558 Tokyo, Japan

3) Laboratoire d'Etude des Microstructures (LEM) UMR 104 ONERA-CNRS, BP 72, 29 avenue de la Division Leclerc, 92322 Chatillon Cedex, France

4) IPCMS, CNRS-UMR 7504, ULP-ECPM, BP 43, 23 rue du Loess, F-67034 Strasbourg Cedex 2, France

* Present address :

Université de Sherbrooke, Chemical and Biotechnological Engineering,

2500 Bd. de l'Université,

Québec, J1K 2R1, Canada.

** Present address :

GPM UMR 6634 CNRS

UFR Sciences et Techniques

Avenue de l'Université - BP12

76801 Saint Etienne du Rouvray, France

Corresponding author

Prof. Christian Ricolleau

Laboratoire Matériaux et Phénomènes Quantiques

Université Paris 7 - CNRS

Case 7021

75205 PARIS cedex 13, France

Tel : 33 1 57 27 62 45

Fax : 33 1 57 27 62 41

E-mail : christian.ricolleau@univ-paris-diderot.fr

Running head : Cold FEG and TEM corrector : first results

Abstract

The performances of a newly developed 80 - 200 kV cold field emission gun (CFEG) transmission electron microscope (TEM), integrating a spherical aberration corrector for TEM image-forming lens, have been evaluated. To begin, we show that the stability of both emission and probe currents makes the use of this new cold-FEG much friendlier. Energy spread of electrons emitted from CFEG has been measured as a function of emission current and shows a very last 0.26 eV energy resolution at 200 kV and even 0.23 eV at 80 kV. The combination of the cold FEG and the CEOS aberration corrector, associated to enhanced mechanical and electrical stabilities of this new microscope, allows reaching a point resolution of 75 pm at 200 kV and 80 pm at 80 kV. This unseen point resolution at 200 kV has allowed us to study the structure of CoPt nanoparticles by observing direct images of their atomic arrangement along high indexes zone axis. We have evidenced the presence of defects in these nanostructures which are not parallel to the electron beam. The precise stoichiometry of two iron oxides, FeO and Fe_2O_3, has been determine from the analysis of iron valence state which was determined from the direct analysis of EELS fine structures spectrum of the two oxides.

1. Introduction

Investigate the atomic scale structure and chemistry of nanomaterials is of primary importance for understanding their fascinating properties. In that regards, Transmission Electron Microscope (TEM) is one of the most complete characterization tools, because it gives access to morphological, structural and chemical information on individually analyzed nano-objects [1-5]. Recently, the development of the aberration correctors [6-9] and highly coherent electron sources [10-12] has boosted the impact of electron microscopy on the characterization of matter at the atomic scale. Indeed, the last generation of instruments attains picometer-order spatial resolution [13-15], with an energy resolution of tenth of an eV [10-12]. Both, high resolution imaging and analytical microscopy have enormously benefited from the technological advances of electron microscopes, resulting in enhanced structural and chemical analysis of nanomaterials [16-20]. Among the electron sources with a narrow energy spread, the high brightness of Cold Field Emission Guns (CFEG) is a tremendous advantage for the study of nanomaterials, in which poor elastic and inelastic signals emitted by small volumes of matter are key limiting factors. So far, highly coherent electron waves emitted from CFEG technology was applied to electron holography observation [21] and the analysis of EELS fine structures [22]. Additionally, the possibility to produce smaller and sharper electron probe with a much larger probe current is efficiently used for both STEM imaging [20, 23] and atomic resolution electron energy loss spectroscopy [24].

The present work describes the performances of an unseen 80 – 200 kV microscope, employing a CFEG and an aberration-corrected objective lens. The capabilities of this

instrument were used to determine the surprising three-dimensional morphology of bimetallic nanoparticles and differentiate the iron valence state in iron oxide nanoparticles.

2. Methods

$Co_{50}Pt_{50}$ nanoparticles (NPs) were grown on [001] NaCl substrate at 400°C. They were produced by pulsed laser deposition (PLD) in a high vacuum chamber [25, 26]. The pressure in the chamber is better than 10^{-9} Pa. A typical target–substrate configuration is used to deposit separately the two metals by PLD using a KrF excimer laser at 248 nm with pulse duration of 25 ns at repetition rates in the range of 1–20 Hz. The laser energy can be chosen in the range of 150–250 mJ, depending on the ablation threshold of the selected target. The sample was obtained by alternated irradiation of the pure Co and Pt metal targets to produce the plasma of each metal. The deposition rate of each element was controlled by an *in situ* quartz crystal monitor. To ensure a good homogeneity of the film, the deposited thickness corresponding to two successive steps (one Co and one Pt) was set to 0.1 nm. The total nominal thickness of the CoPt granular film was 1 nm. After the synthesis, the sample was covered by a 5 nm thick layer of amorphous carbon using the same PLD set-up, in order to perform carbon replica. This replica was then done by dissolution of NaCl in water while recovering the CoPt NPs and the carbon film on a 3 mm Cu commercial TEM grid. TEM experiments are described in details in the results section.

3. Results and discussions

Intrinsic performances of the cold field emission gun.

The CFEG developed in this work, uses a tungsten single crystal emitter with a <310> oriented axis. In order to keep high vacuum level in vicinity of the emitter, three non-evaporative getter (NEG) pumps are installed in the gun chamber [27]. Total evacuation speed of the NEGs corresponds to 300 (= 3 x 100) L/s. The vacuum in the accelerating tube is evacuated by 200 L/s sputter ion pump (SIP). Additionally, two intermediate chambers are designed using small orifices, in order to create a differential pumping system between gun chamber and column. These intermediate chambers are also evacuated by 20 L/s and 30 L/s SIPs, respectively [27]. The newly designed evacuation system can provide a vacuum better than $5x10^{-9}$ Pa, at the bottom of the accelerating tube. Owing to high quality of the vacuum, high stabilities of both emission and probe currents are expected. Figure 1 shows variations of emission and probe currents after flashing procedure of the tip. Decay rate of probe current was less than 5 % in the first 2 hours after flashing. Since the probe current takes only into account electrons emitted by the (310) facets on the tungsten tip, the probe current is more stable than total emission current [28].

Figure 2a shows zero-loss peak measurements at various emission current conditions measured at 200 kV, obtained with a Quantum ER Gatan Imaging Filter. The energy spread of the electron source is commonly defined by the full width at half maximum (FWHM) of the zero-loss peak, measured without specimen. The energy spread depends on the emission current due to the statistical Coulomb effect [29, 30]. The energy spread varies from 0.26 eV with an emission current of 0.1 μA to 0.4 eV in normal emission current conditions (20μA). These values were measured by using an entrance aperture

of 2.5 mm width and the acquisition time was set to 0.1 s. As illustrated in Figure 2b, the energy resolution measurements are even better with an accelerating voltage of 80 kV, since the energy spread ranges from 0.35 eV in normal emission current conditions to 0.23 eV with an emission current of 0.1 μA. The smallest energy spread obtained here is close to the theoretical value at the emitter surface (0.22 eV) [31]. This result shows that the high-voltage stability ($5x10^{-7}$ min^{-1} peak-to-peak fluctuation) is high enough to maintain the energy spread of the CFEG.

Microscope performances.

The objective lens of the TEM used in this experiment has inherent optical performances as listed in Table 1. In this newly developed TEM, a CEOS hexapole type spherical aberration corrector [7] was employed. Therefore, the final spherical aberration coefficient (C_s) can be tuned from – 0.1 mm to + 0.5 mm with a precision of about 1 μm. The lens excitation current of objective lens has a stability of $5x10^{-7}$ min^{-1} in peak-to-peak fluctuation. To evaluate the aberrations of the image-forming system, a diffractogram tableau [32] with a maximum tilt angle of 20 mrad was employed (Fig. 3a), using a thin amorphous carbon film as a specimen. The phase diagram calculated from the diffractogram tableau (Fig 3b) shows that the aberrations were well collected and the phase shift due to the objective lens aberrations was less than λ/4 in an angular range up to 25 mrad. Figure 3c shows a list of residual aberrations calculated in the procedure.

Figure 4a demonstrates the achieved point resolution of the microscope in these imaging conditions. A high resolution image of a carbon film was doubly exposed with

small shift of field of view induced by projector alignment deflector. The Fourier transform of this image gives the well known Young's fringes pattern which shows a point resolution of 75 pm. This resolution was measured with the commonly used minimum contrast level of 13.5 % [14, 33, 34]. Such a performance is close to the theoretical limit for a 200 kV TEM. Figure 4b shows the Fourier transform of a lattice image of a gold single crystal in [100] zone axis orientation. This image highlights that the microscope attains a lattice resolution of 46 pm, since the (048) reflection of the gold lattice is clearly observed. Figure 4c shows the Young's fringes pattern obtained with similar optical parameters at 80 kV. In spite of this low voltage condition, the point resolution of the microscope reaches 80 pm. The possibility to maintain sub-angstrom imaging resolution with an energy resolution below 0.4 eV at 80 kV opens many possibilities for the atomic scale characterization of beam sensitive materials.

Application data:

Structural analysis of CoPt nanoparticles with the sub-angstrom resolution.

To summarize the advantages of an image corrector and a CFEG for the structural study of metallic clusters, it is useful to compare the contrast transfer function (CTF) with and without these optical elements. High-resolution imaging on a microscope not corrected for spherical aberration is limited by its resolution (Fig. 5a). Indeed, comparing the bandwidth of the contrast transfer function (CTF) with the values of typical d_{hkl} in metals, shows that only the planes with the lowest indices can be resolved with an aberration uncorrected microscope. Consequently, the conditions of orientation for which one can observe the structure of a metal nanoparticle is limited to a few zone axes

(only [001] and [110] for face centered cubic (FCC) systems, Fig. 5a). It is thus difficult to determine by HRTEM the structure of a large number of nanoparticles when working on randomly oriented clusters. This limitation is a hindrance for the study of the structural properties of nanoparticles, which requires statistical results on the structure of single particles according to their size and composition. Other TEM techniques, such as nanobeam diffraction or STEM-NBD [35] are then more adapted for the study of size effect in nano-objects [36, 37].

By dividing by 10^3 the spherical aberration coefficient of the objective lens, a C_s -corrector obviously improves microscope resolution. However, beam coherency and microscope stability must be also optimized to reach sub-angstrom resolution and improve signal to noise ratio in the high spatial frequency range. Indeed by minimizing the damping of the envelope functions, the reduction of both electron energy dispersion and mechanical vibration allow a sub-angstrom information transfer limit (Fig. 5b). Thus, high-resolution imaging is not limited any more for the structural study of metal nanoparticles randomly oriented on a substrate: today one can resolve many more inter-reticular distances (Fig. 5b) and thus display the structure of nanoalloys in many more orientations. This major advantage is illustrated in figure 5b, in which the structure of a CoPt nanoparticle in [114] zone-axis orientation is directly observed on the C_s corrected high resolution image and an information transfer up to the -440 reflection (65 pm) is reported on the Fourier transform. The comparison of figure 5a and 5b shows another significant advantage of corrected microscopy for studying nano-objects. Indeed the absence of delocalization contrast on C_s-corrected images allows a better visualization of nanoparticle surfaces, which opens many avenues for the characterization of catalytic nanoparticles, for which the structure and composition of

the surface are crucial information.

CoPt NPs in epitaxial relationship with an [001] NaCl substrate were fabricated by PLD (see method section). The [002] direction of the FCC structure of the NPs is then parallel to the [002] axis of NaCl and perpendicular to the substrate plane. The [220] directions of the NPs structure are in the plane of the substrate and parallel to the [200] and [020] directions of NaCl. We can observe two populations of NPs (Fig. 6a): the first one is constituted of squared shape NPs in the plane of the substrate and the other one has a triangular shape. According to electron tomography (not shown here) and HRTEM experiments (Fig. 6b), the 3D morphology of the nanosquares corresponds in fact to a truncated octahedron morphology in good agreement with the Wulff-Kaichew equilibrium shape of supported CoPt NPs on a low interacting support [38].

Concerning the triangular shaped NPs, two cases are observed: the first ones are oriented along the [002] zone axis and correspond to truncated octahedron which are not symmetrically truncated in the [200] and [$\bar{2}$00] directions. This configuration corresponds to NPs that have not fully reached their equilibrium shape. The second case is shown on figure 6c. On this example, the upper right side of the NP is oriented along the [114] direction whereas the lower left side is oriented along the [$\bar{1}$01] direction as indicated in the right and left inserts respectively. This configuration was observed on around 6 % of the whole NPs assembly. Giving the as-grown orientation relationship between NPs and the NaCl substrate, the initial direction of the NPs perpendicular to the substrate have to be [002]. The carbon replica technique can induce misorientations of the NPs assembly with respect to the growing directions. In the example shown here, the misorientation corresponds to the angle between the [002] and the [114] directions (19.47°).

In very small objects, grain boundaries are unlikely to exist. Among all kind of defects in the FCC structure, the one that implies orientation change of crystal is the twin boundary (*i.e.* the so-called $\Sigma = 3$ {111} boundary). Let first examine the case of a twin boundary oriented along the [110] direction, as conventionally observed. This defect corresponds to two crystals, namely crystal 1 and 2 respectively, that are in mirror symmetry with respect to the (111) plane. The corresponding reciprocal lattices of the two twinned crystals in projection along the [110] direction are shown in figure 7 (crystals 1 and 2 are in black and red respectively). In conventional high resolution imaging, the images are obtained along the [110] direction because it is the only one where the interface plane is parallel to the electron beam and exhibits lattice distances that can be resolved.

The experimental example shown in figure 6c corresponds to two twinned crystals observed in a completely different direction. Due to epitaxial relationship, crystal 1 is oriented along the [002] zone axis. According to figure 7, the $[\bar{2}02]$ direction of crystal 2 is oriented at 19.47° of the [002] direction of crystal 1. However, due to the disorientation of the C film during the replica process, the zone axis orientation of crystal 1 is [114] and, as we have seen above, the [002] direction is exactly at 19.47° of the [114] direction. Therefore, if crystal 1 is oriented along the [114] direction, the direction of crystal 2 that is parallel to the electron beam is the $[\bar{2}02]$ direction, as observed on the example of figure 6c. This structural analysis was only possible because of the ability of the aberration-corrected microscope to resolve the 0.11nm atomic distances observed in the CoPt crystal oriented along the [114] zone axis. This analysis was confirmed by electron tomography experiment. A NP exhibiting a similar morphology has been isolated on a 3D tomogram. The Figure 6d shows (x, z) slice of

the 3D reconstruction of the particle (the substrate plane is defined as (x,y) and the z direction is perpendicular to the substrate). On this cross-section view, the substrate plane is indicated by a grey line and the nanoparticle is in blue. This image shows that the NP exhibits an angel wing-like shape with an angle of 120° between the lower and the upper parts of the NP. It appears from figure 7, that the angle between the (200) planes of the two faulted crystal is equal to 109.47°. It is well known in tomography, that due to the missing wedge, the reconstructed 3D objects are elongated perpendicularly to the plane of the substrate. This effect is characterized by an elongation factor e [39]. In our experiment, this elongation factor is equal to 1.25. If we take into account of this elongation in a simple geometric model, the angle between the (200) planes of the twinned crystals, is equal to 120°, as experimentally observed by electron tomography. Therefore, the breaking between the lower and the upper parts of the NP, giving rise to the surprising angel-wing like morphology is due to the presence of a $\Sigma = 3$ {111} twin boundary.

Analysis of iron valence state in iron oxides

Iron oxides are nowadays used in various industrial and biomedical applications such as heterogeneous catalysis, medical imaging and therapy. The interest for these oxides originates from the richness of their electronic, structural and chemical properties. For these different applications, it is important to be able to discriminate among the different oxides down to the nanoscale.

Four iron oxides are commonly encountered: hematite (α-Fe_2O_3), maghemite (γ-Fe_2O_3), magnetite (Fe_3O_4) and wüstite (FeO). Hematite and wüstite are antiferromagnetic

insulators. In the former, the Fe^{3+} ions are bounded, in a nearly-perfect octahedral configuration to the O^{2-} ions while in the latter, the Fe^{2+} are in perfect octahedral sites. As for magnetite and maghemite, they are ferrimagnetic compounds. They have an inverse spinel structure in which the Fe^{2+} and Fe^{3+} ions for magnetite and Fe^{3+} ions in maghemite sit in distorted octahedral and tetrahedral sites. To probe the rich electronic and structural configurations encountered in iron oxides, EELS at the oxygen K and iron $L_{2,3}$ edges has proven to be a powerful technique.

The O K-edge is composed of a pre-peak followed by a broad edge extending at higher energy losses. These features result from the excitations of the O 1s electrons to empty states of O p symmetry (hybridized O 2p and Fe 3d states for the pre-peak and hybridized O 2p and Fe 4sp states for the extended feature) [40]. As for the iron $L_{2,3}$ edges, it is dominated by excitation of Fe 2p electrons to 3d symmetry orbitals. In ferric iron, the Fe $L_{2,3}$ edge corresponds to an electronic excitation from an initial Fe 2p6 3d5 state to a final Fe 2p6 3d6 state while in ferrous iron, the excitation is from a Fe 2p6 3d6 state to a Fe 2p6 3d7 state. It presents two prominent peaks labelled $L_3(2p_{3/2})$ and $L_2(2p_{1/2})$ separated by about 13 eV resulting from the spin-orbit splitting of the iron 2p energy level.

Early EELS studies of the different phases of iron oxides relied on the L_3/L_2 white-line intensity ratio to monitor the iron valence state of the oxides. This ratio varies with the transition metal d-band occupancy [41]. It has also been shown that a change in d-band occupancy induces a chemical shift of the L_3 edge maximum.

With the increase in energy resolution giving access to the near-edge fine structures (ELNES) in EELS spectra, it has been shown that the Fe L_2 and L_3 and O K edges display multiplets structures within the edges. These peak-splittings and intensity

redistribution have been attributed to crystal-field and electronic effects [40, 42] and reflect the oxidation state, site symmetry and local bonding of the ions present in the oxide phase under investigation. The ELNES fingerprinting of these edges can thus be used to unambiguously determine the oxide phase under investigation [22].

Figure 8 compares the ELNES of Fe $L_{2,3}$ and O K edges acquired on α-Fe_2O_3 and FeO nanocrystals (Furuuchi Chemical Corporation™) in the STEM mode with the microscope operating at 200 kV and with an emission current of 20 µA. Each spectrum was obtained by summing 50 spectra each acquired in 1s. The 50 spectra were realigned among themselves before summing. During spectrum acquisition, the dualEELS capability of the GIF Quantum® was enabled to obtain simultaneously the low and core loss regions of the EELS. Having the low loss spectra allows precise measurements of any chemical shift and peak-splitting due to crystal-field and/or electronic effects.

In hematite, the ELNES of Fe L_3 displays a characteristic strong pre-peak located at 709.7 eV while the maximum of the main peak is at 711.3 eV. In comparison, the maximum of Fe L_3 in wüstite is shifted to 710 eV and though asymmetric, it presents no peak-splitting (Figure 8a). Pertaining to the O K edge ELNES, hematite and wüstite display different pre-peak structures. In hematite, a strong split pre-peak around 532 eV with a splitting of about 1.4 eV is measured while in wüstite, only a broad pre-peak centered at about 531 eV is detected (Figure 8b).

These results show that the high brightness and high-voltage stability of the CFEG gun enable detailed analysis EELS fine structures retrieved with sub-nanometer resolution. Exemplified on iron oxides here, this approach can be extended to a wide variety of nanosystems.

4. Conclusion

The electron microscope describes in this paper is the first commercial instrument combining both a cold field emission electron source and an aberration corrector of the objective lens. We have shown the very good stability of both emission and probe current thanks to a new design of the vacuum system for the gun chamber including non evaporating getter pumps. The combination of the JEOL cold FEG and the CEOS aberration corrector, associated to enhanced mechanical and electrical stabilities of the TEM which is commercialized as JEM-ARM200F microscope by JEOL, allows reaching a point resolution of 75 pm at 200 kV and 80 pm at 80 kV. In addition, the high brightness of the cold FEG substantially improved imaging sensitivity that is essential for quantitative high resolution imaging. We have shown that sub-angstrom imaging is of great benefit for understanding the structural properties of nanomaterials, because it is now possible to observe crystals and defects along high index zone axis orientation. The atomic structure of a twin boundary in a CoPt nanoparticle observed along an uncommon [114] zone axis was analyzed. We have also demonstrated that the performances of the microscope can be exploited for studying the electronic properties of materials, as for example, the valence state of the metal in metallic oxides. We have shown the direct determination of the α-Fe_2O_3 and FeO phases, by resolving the fine structure of the iron $L_{2,3}$ and oxygen K edges. The energy resolution below 0.4 eV combined with the DualEELS mode allows studying simultaneously the fine structure and the possible chemical shift of absorption edges.

Acknowledgments

Financial support from ANR within ANR-07-NANO-018-04 (ETNAA) is gratefully acknowledged.

References

1. Kirkland a I 2007. *Nanocharacterisation*. (Royal Society of Chemistry, Cambridge).

2. Reimer L 1997. *Transmission Electron Microscopy*. (Springer, Berlin).

3. Shindo D and Hiraga K 1998. *High-Resolution Electron Microscopy for Materials Science*. (Springer Verlag Tokyo).

4. Wang Z L 2000. Transmission Electron Microscopy of Shape-Controlled Nanocrystals and Their Assemblies. *The Journal of Physical Chemistry B* **104**, 1153-1175.

5. Willams B and Barry Carter C 1996. *Transmission Electron Microscopy*. (Plenum, New York).

6. Beck V D 1979. A hexapole spherical aberration corrector. *Optik* **53**, 241-255.

7. Haider M, Uhlemann S, Schwan E, Rose H, Kabius B and Urban K 1998. Electron microscopy image enhanced. *Nature* **392**, 768-769.

8. Krivanek O L, Dellby N and Lupini a R 1999. Towards sub-Angstrom electron beams. *Ultramicroscopy* **78**, 1-11.

9. Orloff J 2009. *Handbook of Charged Particle Optics* (CRC Press).

10. Browning N D, Arslan I, Erni R, Idrobo J C, Ziegler A, Bradley J, Dai Z, Stach E A and Bleloch A 2006. Monochromators and aberration correctors: Taking EELS to new levels of energy and spatial resolution. In: *EMAG-NANO 2005: Imaging, Analysis and Fabrication*

on the Nanoscale, eds. Brown P D, Baker R and Hamilton B, pp. 59-64, (Iop Publishing Ltd, Bristol).

11. Kimoto K, Ishizuka K, Asaka T, Nagai T and Matsui Y 2005. 0.23 eV energy resolution obtained using a cold field-emission gun and a streak imaging technique. *Micron* **36**, 465-469.

12. Kimoto K, Kothleitner G, Grogger W, Matsui Y and Hofer F 2005. Advantages of a monochromator for bandgap measurements using electron energy-loss spectroscopy. *Micron* **36**, 185-189.

13. Urban K 2008. Studying Atomic Structures by Aberration Corrected Transmission Electron Microscopy. *Science* **321**, 506-510.

14. Kisielowski C, Freitag B, Bischoff M, Van Lin H, Lazar S, Knippels G, Tiemeijer P, Van Der Stam M, Von Harrach S, Stekelenburg M, Haider M, Uhlemann S, Müller H, Hartel P, Kabius B, Miller D, Petrov I, Olson E A, Donchev T, Kenik E A, Lupini a R, Bentley J, Pennycook S J, Anderson I M, Minor a M, Schmid a K, Duden T, Radmilovic V, Ramasse Q M, Watanabe M, Erni R, Stach E A, Denes P and Dahmen U 2008. Detection of Single Atoms and Buried Defects in Three Dimensions by Aberration-Corrected Electron Microscope with 0.5-Å Information Limit. *Microscopy and Microanalysis* **14**, 469-477.

15. Takayanagi K, Kim S, Lee S, Oshima Y, Tanaka T, Tanishiro Y, Sawada H,

Hosokawa F, Tomita T, Kaneyama T and Kondo Y Electron microscopy at a sub-50Â pm resolution. In: *Journal of Electron Microscopy*, pp. S239-S244).

16. Alloyeau D, Ding B, Ramasse Q, Kisielowski C, Lee Z and Jeon K-J Direct imaging and chemical analysis of unstained DNA origami performed with a transmission electron microscope. *Chemical Communications* **47**, 9375-9377.

17. Alloyeau D, Freitag B, Dag S, Wang L W and Kisielowski C 2009. Atomic-resolution three-dimensional imaging of germanium self-interstitials near a surface: Aberration-corrected transmission electron microscopy. *Phys. Rev. B* **80**, 014114.

18. Herzing a A, Watanabe M, Edwards J K, Conte M, Tang Z-R, Hutchings G J and Kiely C J 2008. Energy dispersive X-ray spectroscopy of bimetallic nanoparticles in an aberration corrected scanning transmission electron microscope. *Faraday Discussions* **138**, 337-351.

19. Girit Ã a Ã, Meyer J C, Erni R, Rossell M D, Kisielowski C, Yang L, Park C-H, Crommie M F, Cohen M L, Louie S G and Zettl A 2009. Graphene at the Edge: Stability and Dynamics. *Science* **323**, 1705-1708.

20. Krivanek O L, Chisholm M F, Nicolosi V, Pennycook T J, Corbin G J, Dellby N, Murfitt M F, Own C S, Szilagyi Z S, Oxley M P, Pantelides S T and Pennycook S J 2010. Atom-by-atom structural and chemical analysis by annular dark-field electron microscopy.

Nature **464**, 571-574.

21. Tonomura A 1987. Applications of electron holography. *Rev. Mod. Phys.* **59**, 639-669.

22. Chen S-Y, Gloter A, Zobelli A, Wang L, Chen C-H and Colliex C 2009. Electron energy loss spectroscopy and ab initio investigation of iron oxide nanomaterials grown by a hydrothermal process. *Phys. Rev. B* **79**, 104103.

23. Konno M, Suzuki Y, Inada H and Nakamura K 2010. Application of 80-200 kV Aberration Corrected Dedicated STEM With Cold FEG. In: *Electron Microscopy and Analysis Group Conference 2009*, (Iop Publishing Ltd, Bristol).

24. Trasobares S, López-Haro M, Kociak M, March K, De La Peña F, Perez-Omil J A, Calvino J J, Lugg N R, D'alfonso a J, Allen L J and Colliex C 2011. Chemical Imaging at Atomic Resolution as a Technique To Refine the Local Structure of Nanocrystals. *Angewandte Chemie International Edition* **50**, 868-872.

25. Alloyeau D, Langlois C, Ricolleau C, Le Bouar Y and Loiseau A 2007. A TEM *in situ* experiment as a guideline for the synthesis of as-grown ordered CoPt nanoparticles. *Nanotechnology* **18**, 375301.

26. Alloyeau D, Ricolleau C, Langlois C, Le Bouar Y and Loiseau A 2010. Flash laser annealing for controlling size and shape of magnetic alloy nanoparticles. *Beilstein Journal of*

Nanotechnology **1**, 55-59.

27. Kohno Y, Okunishi E, Tomita T, Ishikawa I, Kaneyama T, Ohkura Y, Kondo Y and Isabell. T 2010. Development of a Cold field-Emission Gun for a 200 kV Atomic Resolution Electron Microscope. *Microscopy and Analysis Nanotechnology* **24**.

28. Keigo K, Souichi K, Takashi O and Shigeru K Stabilization of a tungsten <310> cold field emitter. *Journal of Vacuum Science & Technology B: Microelectronics and Nanometer Structures* **28**, L55-L60.

29. Jansen G H 1990. *Coulomb interaction in particle beams*. (Academic press inc.).

30. Tiemeijer P C 1999. Measurement of Coulomb interactions in an electron beam monochromator. *Ultramicroscopy* **78**, 53-62.

31. Hawkes P 2009. *Advances in Imaging and Electron Physics*. (Elsevier, Amsterdam).

32. Zemlin F, Weiss K, Schiske P, Kunath W and Herrmann K H 1978. Coma-free alignment of high resolution electron microscopes with the aid of optical diffractograms. *Ultramicroscopy* **3**, 49-60.

33. Kaiser U, Biskupek J, Meyer J C, Leschner J, Lechner L, Rose H, Stã¶Ger-Pollach M, Khlobystov a N, Hartel P, Mã¼Ller H, Haider M, Eyhusen S and Benner G Transmission electron microscopy at 20 kV for imaging and spectroscopy. *Ultramicroscopy* **111**,

1239-1246.

34. D. A. Blom, L. F. Allard, M. A. O'keefe and Mishina S 2009. High Resolution Imaging with an Aberration Corrected JEOL 2200FS-AC STEM/TEM. *Microscopy and microanalysis* **11**, 548.

35. Alloyeau D, Ricolleau C, Oikawa T, Langlois C, Le Bouar Y and Loiseau A 2008. STEM nanodiffraction technique for structural analysis of CoPt nanoparticles. *Ultramicroscopy* **108**, 656-662.

36. Alloyeau D, Ricolleau C, Mottet C, Oikawa T, Langlois C, Le Bouar Y, Braidy N and Loiseau A 2009. Size and shape effects on the order-disorder phase transition in CoPt nanoparticles. *Nature Materials* **8**, 940-946.

37. Sato K, Hirotsu Y, Mori H, Wang Z and Hirayama T 2005. Long-range order parameter of single $L1_0$-FePd nanoparticle determined by nanobeam electron diffraction: Particle size dependence of the order parameter. *Journal of Applied Physics* **98**, 024308.

38. Henry C 2005. Morphology of supported nanoparticles. *Progress in Surface Science* **80**, 92-116.

39. Alloyeau D, Ricolleau C, Oikawa T, Langlois C, Le Bouar Y and Loiseau A 2009. Comparing electron tomography and HRTEM slicing methods as tools to measure the thickness of nanoparticles. *Ultramicroscopy* **109**, 788-796.

40. C. Colliex, T. Manoubi and C. Ortiz 1991. Electron-energy-loss-spectroscopy near-edge fine structures in the iron-oxygen system. *Phys. Rev. B* **44**, 11402.

41. Leapman R D, Grunes L A and Fejes P L 1982. Study of the $L_{2,3}$ edges in the 3d transition metals and their oxides by electron-energy-loss spectroscopy with comparisons to theory. *Phys. Rev. B* **26**, 614-635.

42. Crocombette J P, Pollak M, Jollet F, Thromat N and Gautier-Soyer M 1995. X-ray-absorption spectroscopy at the Fe L_{2,3} threshold in iron oxides. *Phys. Rev. B* **52**, 3143-3150.

Table 1. Inherent optical performances of objective lens employed in the TEM.

Items	**Performances**	
	200 kV	**80 kV**
Focal length (f_0)	1.9 mm	1.0 mm
Spherical aberration coefficient (C_s)	0.5 mm	0.5 mm
Chromatic aberration coefficient (C_c)	1.1 mm	0.7 mm
Minimum focus step (Δf)	0.25 nm	0.69 nm
Lens current fluctuation (peak-to-peak) (ΔI)	5×10^{-7} /min	5×10^{-7} /min

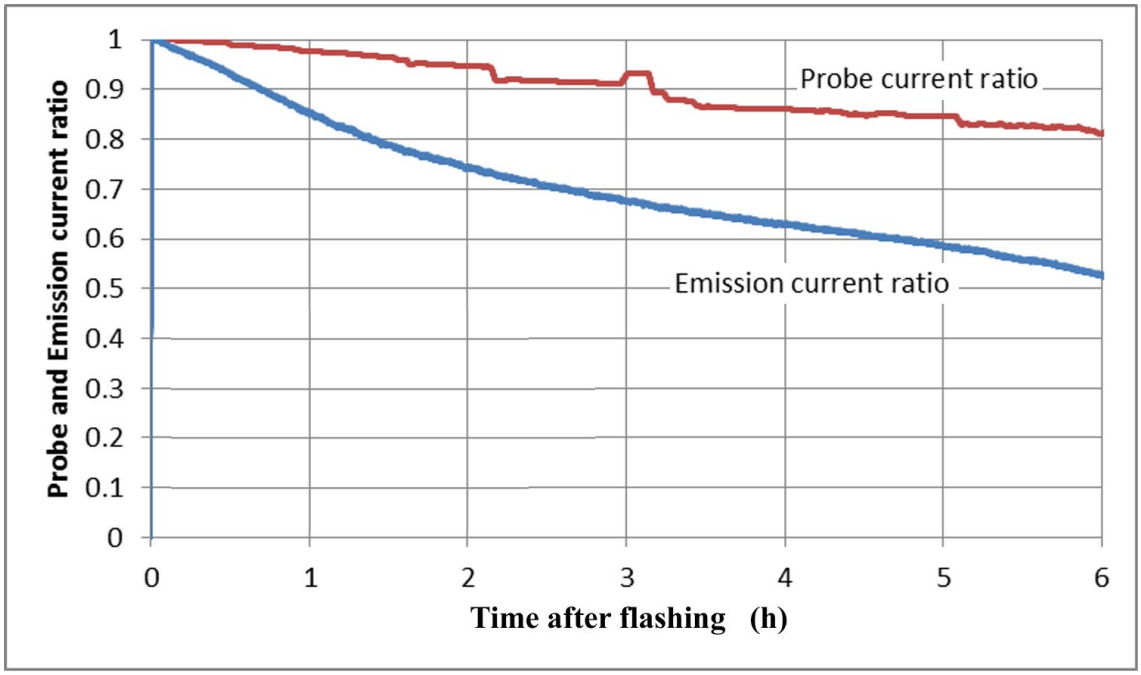

Figure 1 : Normalized variations of emission and probe currents after flashing procedure. Decay rate of probe current was less than 5 % in the first 2 hours after the flashing.

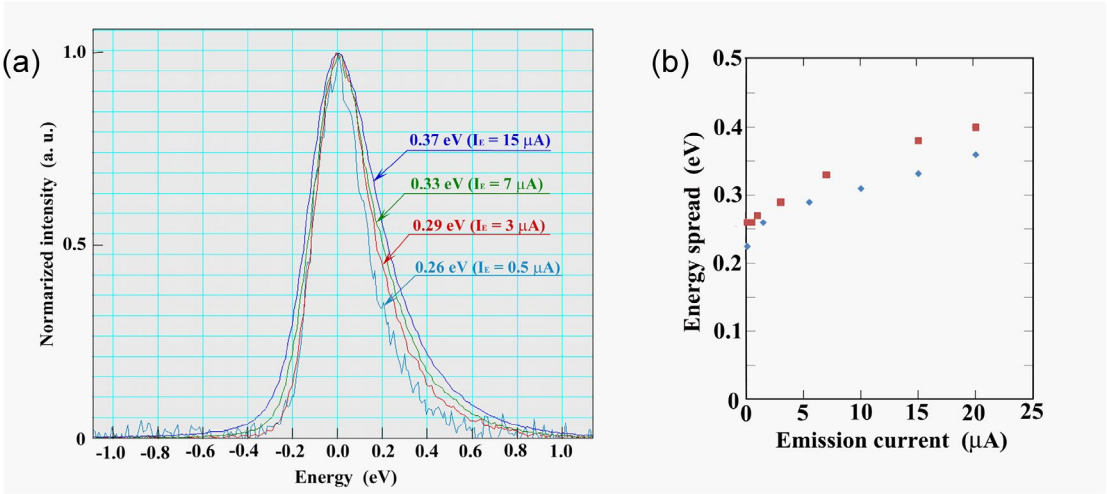

Figure 2 : (a) Measured zero-loss peaks at various emission current (I_E) conditions measured at 200 kV. The energy spread was defined by FWHM of the zero-loss peak. (b) Energy spread as a function of emission current measured at 200 kV (red curve) and at 80 kV (blue curve).

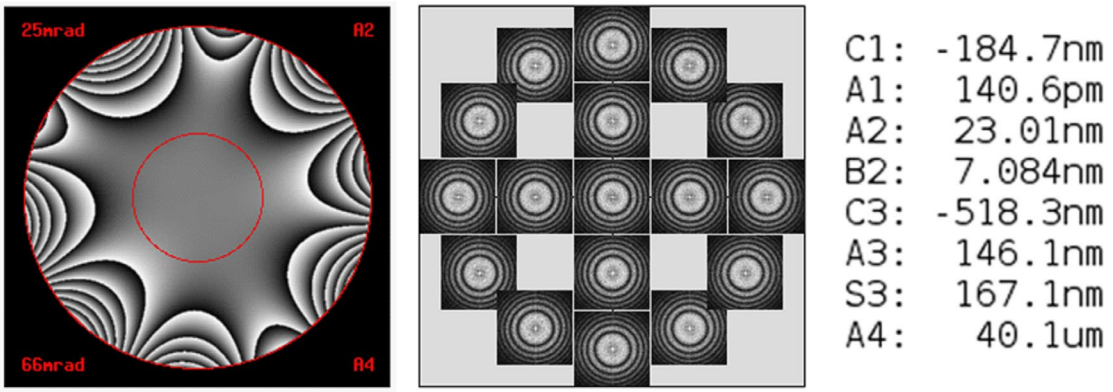

Figure 3 : Spherical aberration correction procedure and residual aberrations. (a) Diffractogram tableau with beam tilting [13]. The maximum tilting angle was 20 mrad. (b) Phase diagram calculated from diffractogram tableau. (c) Calculated residual aberrations from diffractogram tableau.

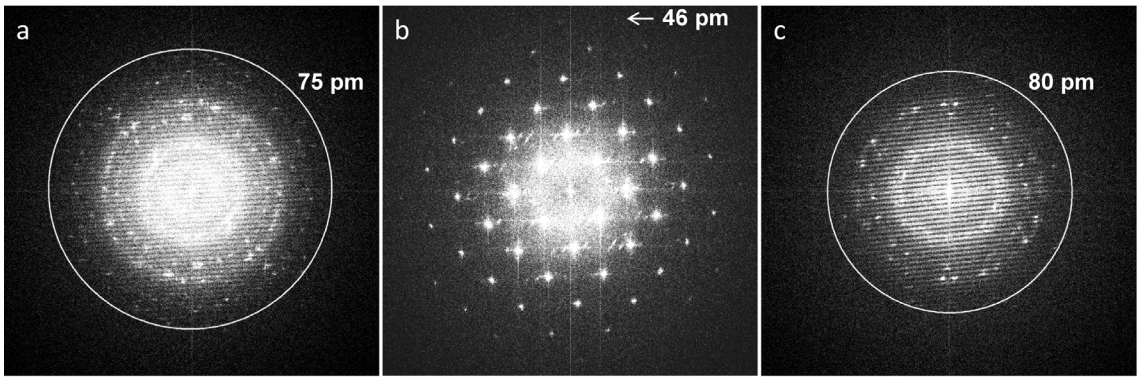

Figure 4 : (a) Young fringes pattern obtained at 200 kV showing a point resolution of 75 pm. (b) Fast Fourier transformation (FFT) of a high resolution image obtained at 200 kV on a (100) gold single crystal. The observation of the [048] peak of the gold crystal highlights that the lattice resolution of the microscope is below 50 pm (d_{048} = 0.046nm). (c) Young fringes pattern obtained at 80 kV showing a point resolution of 80 pm. The bottom right inset of (a) and (c), show intensity profiles measured along the white box perpendicular to the Young fringes.

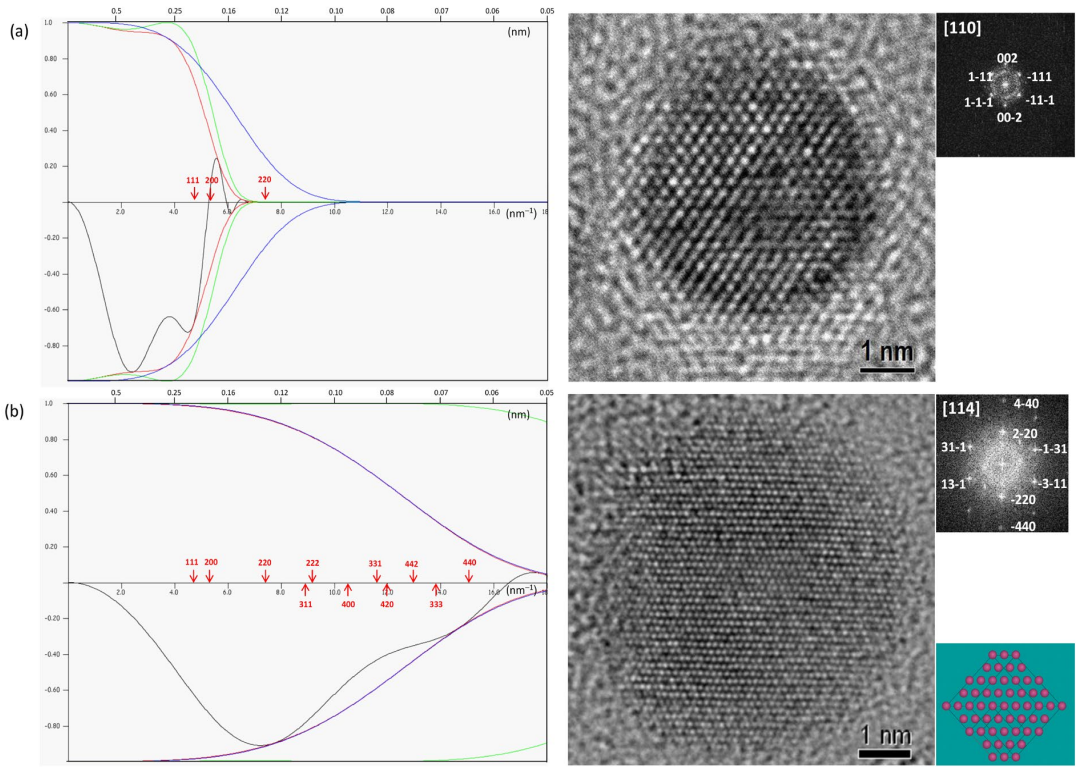

Figure 5 : Total CTF (black curve), corresponds to the product of the CTF $T(\nu)$ by the partial spatial coherence (E_s, green curve) and the partial temporal coherence (E_c, blue curve) envelopes. The red curve corresponds to the total envelope function. These curves are computed for an acceleration voltage of 200kV and the inter-reticular distances from the CoPt system are indicated in red. The HRTEM image of a CoPt nanoparticle acquired under the same optical conditions than the computed CTF. The corresponding power spectrum of the HRTEM image is presented in insert. (a) Microscope with no corrector and a conventional FEG, C_s = 0.5 mm, Δf = – 42 nm (Scherzer focus) and focus spread of 10 nm. CoPt nanoparticle in [110] zone axis orientation. (b) Microscope with a C_s-corrector and a cold FEG electron source. C_s = 0,005 mm, Δf = – 4 nm (Scherzer focus), focus spread of 2.3 nm. CoPt nanoparticle in [114] zone axis orientation.

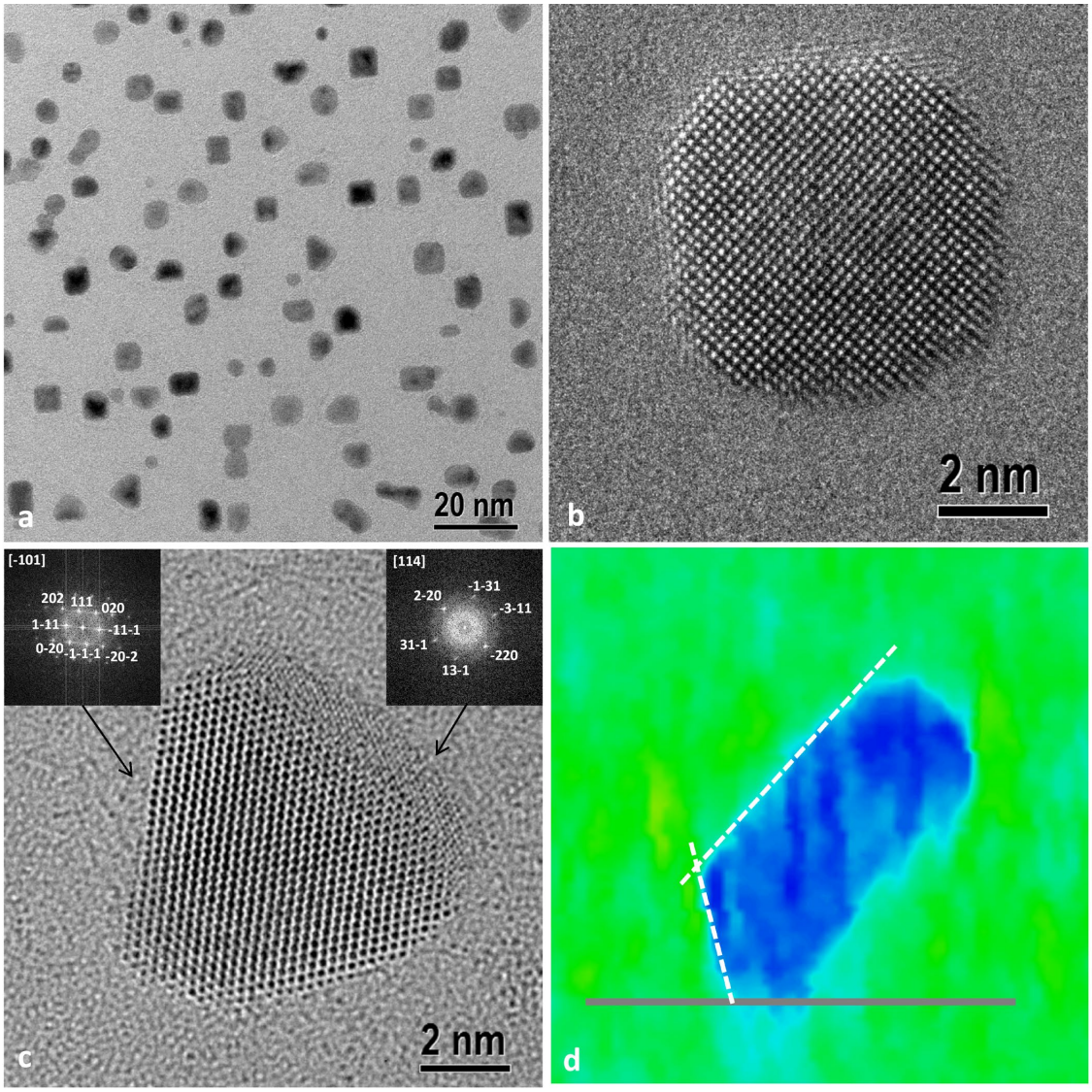

Figure 6 : (a) Bright filed image of as-grown CoPt NPs obtained on a carbon replica. (b) HRTEM image of a CoPt NP oriented along the [002] showing the truncated octahedron morphology. (c) Triangular shaped NP exhibiting the [$\bar{1}$01] and [114] zone axes orientations. (d) 3D shape of the triangular shaped NP obtained by electron tomography showing the angel wing like morphology. CoPt nanoparticle is in blue, vacuum is in green and the substrate plane is outlined by the horizontal grey line.

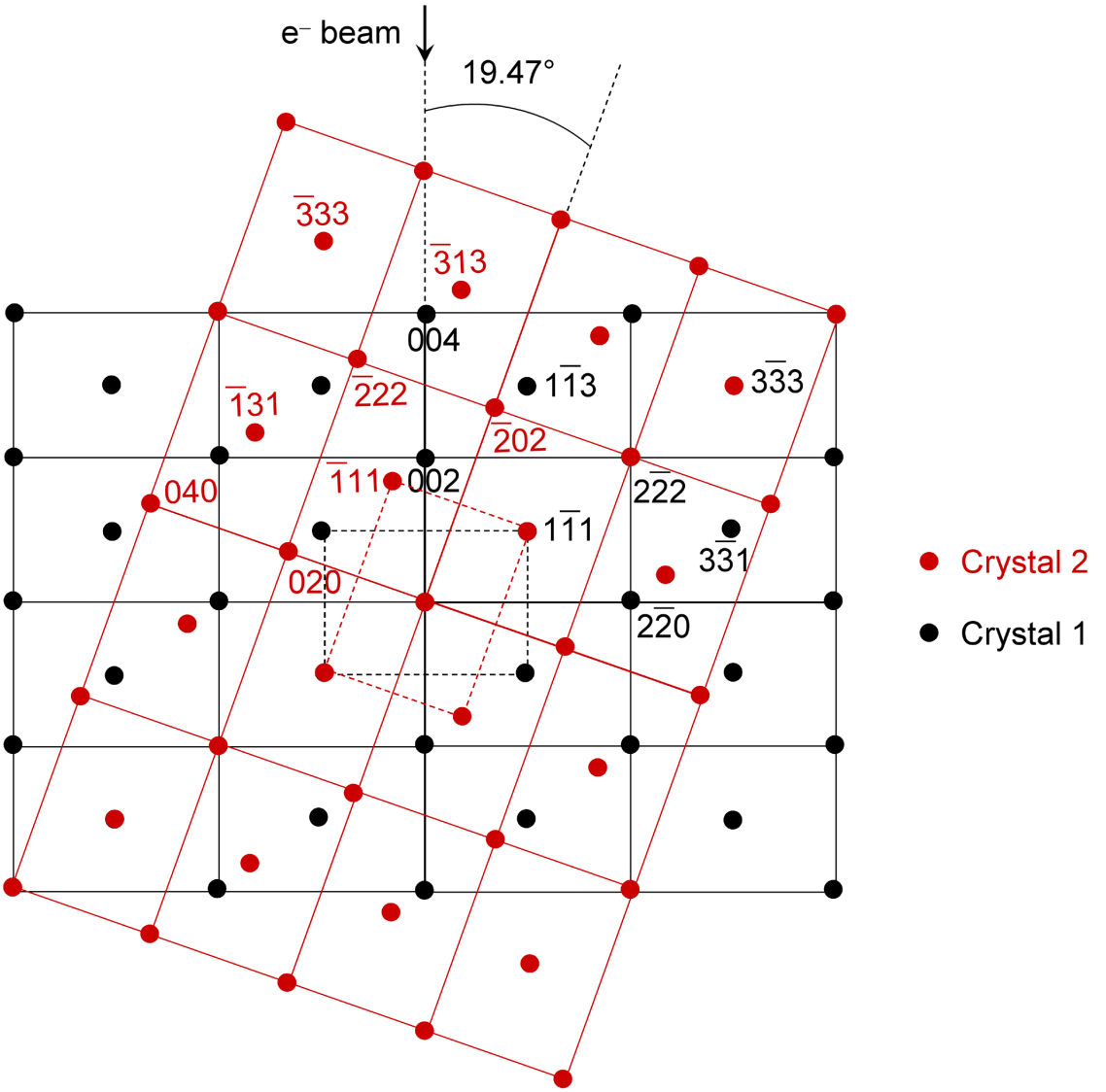

Figure 7 : Reciprocal lattices of two twinned crystals projected along the [110] axis (black colour : crystal 1, red colour : crystal 2). Crystals 1 and 2 are oriented respectively along the [110] and [101] zone axes. The angle between the [002] direction of crystal 1 and the [$\bar{2}$02] direction of crystal 2 is equal to 19.47°.

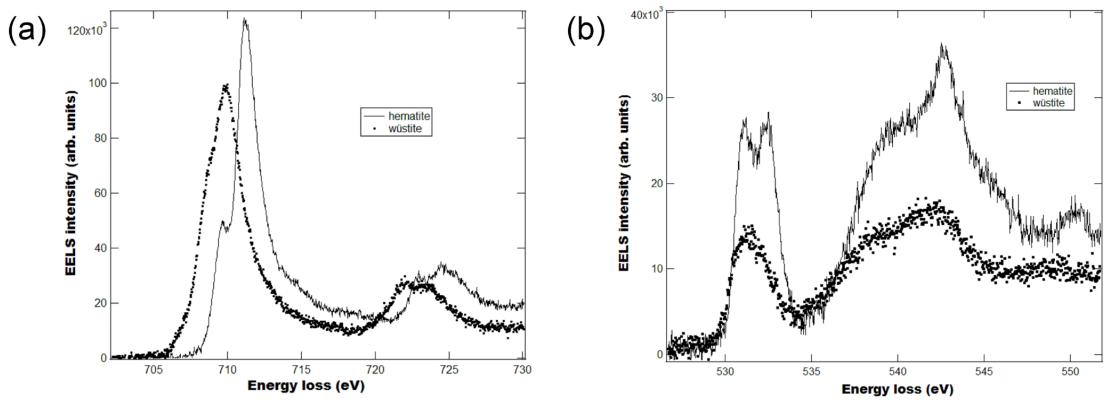

Figure 8: Comparison of (a) the Fe $L_{2,3}$-edge and (b) the O K-edge electron energy-loss near-edge structures of α-Fe_2O_3 (plain lines) and FeO (black dots). The pre-edge background for each edge has been subtracted using a power-law function. The contribution from transitions to the continuum states has not been removed.